Journal of
Experimental and Theoretical Analyses

MDPI

Article

Impact of Sensor Accuracy and Model Calibration on Simulation of Heat Pumps with Refrigerant Leakage Faults

Francesco Pelella [1,*], Adelso Flaviano Passarelli [1], Raffaele Cilento [1], Belén Llopis-Mengual [2], Luca Viscito [1], Emilio Navarro-Peris [2] and Alfonso William Mauro [1]

[1] Department of Industrial Engineering, Università degli Studi di Napoli–Federico II, P.le Tecchio 80, 80125 Naples, Italy; adelsoflaviano.passarelli@unina.it (A.F.P.); raffaele.cilento@unina.it (R.C.); luca.viscito@unina.it (L.V.); wmauro@unina.it (A.W.M.)

[2] Instituto Universitario de Investigación de Ingeniería Energética (IUIIE), Universitat Politècnica de València (UPV), Camino de Vera s/n, 46022 Valencia, Spain; belen.llopis@iie.upv.es (B.L.-M.); emilio.navarro@iie.upv.es (E.N.-P.)

* Correspondence: francesco.pelella@unina.it

Abstract

Soft operational faults can noticeably degrade the performance of heat pumps and influence key monitored variables, emphasizing the need for reliable Fault Detection, Diagnosis, and Evaluation (FDDE) strategies. The BEYOND project tackles this challenge by analyzing simultaneous soft faults using a calibrated simulation model informed by data from a dedicated test rig. Achieving reliable results depends on both accurate measurements and proper model calibration. However, sensor uncertainty and errors in sub-models and correlations calibration can compromise model reliability. This work investigates the influence of measurement accuracy and calibration quality on both experimental variables and simulation outcomes for a residential air-to-water heat pump operating in cooling mode, with particular focus on refrigerant charge estimation. Two sensor configurations—"low accuracy" and "high accuracy"—are assessed, representing commercial- and laboratory-grade instruments, respectively, along with two corresponding calibration strategies. In the low-accuracy case, uncertainties around 10% were found for cooling capacity, energy efficiency ratio, and refrigerant mass flow rate, whereas high-accuracy setups reduced these to approximately 3%. Ultimately, the comparison between experimental and model-derived uncertainties confirms that achieving reliable predictions requires a balanced investment in both high-quality instrumentation and careful model calibration. Overall, this study serves as a crucial tool during the preliminary design of an experimental setup, assisting in the selection of a sensor suite that ensures not only the reliability of secondary variables and KPIs but also a robust and accurate calibration of physics-based models using the acquired experimental data.

Keywords: air-to-water heat pump; fault detection and diagnosis; uncertainty projection; refrigerant charge; modeling

Check for updates

Academic Editors: Marco Rossi and Shuhui Li

Received: 31 March 2026
Revised: 23 April 2026
Accepted: 8 May 2026
Published: 14 May 2026

Copyright: © 2026 by the authors. Licensee MDPI, Basel, Switzerland. This article is an open access article distributed under the terms and conditions of the Creative Commons Attribution (CC BY) license.

1. Introduction

The heating and cooling sector accounts for over 35% of total energy consumption in buildings [1], highlighting the urgent need for more sustainable solutions. Among available technologies, heat pumps stand out as the only viable option currently able to meet regulatory targets for replacing traditional heating systems and achieving decarbonization goals by 2050 [2], thanks to their high efficiency and ability to utilize renewable energy

sources. However, despite recent regulations aimed at minimizing both direct and indirect environmental impacts [3,4], the performance of heat pumps can be significantly reduced by soft faults. Unlike hard faults [5], such as compressor or fan failure, which cause immediate shutdowns, soft faults allow continued operations but with reduced efficiency [6]. If undetected, they can persist over time, leading to increased energy use and decreased performance. Common examples include heat exchanger fouling, refrigerant leakage or overcharge, compressor ageing, valve leakage, and liquid line restrictions. Therefore, to maintain system performance, it is essential to deploy advanced techniques capable of detecting the presence of a fault (FD: Fault Detection), identifying the type of fault (FDD: Fault Detection and Diagnosis), and ultimately evaluating its severity (FDDE: Fault Detection, Diagnosis, and Evaluation). These are especially critical when faults cause degradation beyond acceptable thresholds. Experimental studies play a key role in this context, with two main goals: evaluating how soft faults affect system performance, and identifying the most sensitive variables that can serve as indicators for FDDE.

Several works in the literature have explored these aspects by analyzing the effects of soft faults on key variables of the thermodynamic cycle and by developing numerical models of heat pump system performance under both normal and faulty conditions. Comstock et al. [7], under the ASHRAE 1043-RP project [8], conducted experiments on a centrifugal chiller, collecting detailed measurements of pressure and temperature in both fault-free and faulty conditions. Similarly, Bellanco et al. [9] examined the effects of single soft faults such as refrigerant overcharge, liquid line restriction, evaporator fouling, and compressor valve leakage on the performance of a variable-speed heat pump system, focusing on the coefficient of performance (COP), power consumption, and temperatures/pressures trends. A similar investigation was also conducted by Noel et al. [10], who quantified the normalized impact of individual faults (e.g., heat exchanger fouling, incorrect refrigerant charge) on system key variables such as evaporator superheat, condenser subcooling, condensing and evaporating temperatures, compressor frequency, refrigerant mass flow rate, and electronic expansion valve (EEV) position. Gou et al. [11] reported similar findings for VRV/VRF systems, where long piping often causes "compressor liquid floodback" issues [12], whereas an impact of key hyperparameters on the diagnostic performance of an FDD algorithm was conducted by Guo et al. [13,14].

However, an emerging challenge is the occurrence of multiple simultaneous faults. As shown in Mauro et al. [15] and Llopis-Mengual et al. [16], the coexistence of more than one fault can affect the same variable, leading to synergistic or canceling effects. Hu and Yuill [17,18] also demonstrated how combinations of two to four faults alter system behavior in complex ways, making fault identification harder. These combined effects can create indeterminacy zones, where it becomes impossible to uniquely identify the faults, especially when the uncertainty associated with the instrumentation used is considered [19]. Therefore, the effectiveness of these diagnostic techniques is inherently limited by the quality of the input data and the associated uncertainty.

Addressing these key challenges requires the development of experimental test apparatuses and dedicated new procedures, particularly aimed at accurately evaluating the effects of multiple simultaneous soft faults in heat pump systems. Furthermore, the first step in setting up an experimental setup is to select the appropriate sensor suite to be installed and to determine its measurement uncertainty, since this uncertainty could have a significant impact on both the experimental results and the calibration of simulation models based on these data, as well as on any FDDE algorithms. This issue was specifically addressed in a previous study [20], which demonstrated how sensor uncertainty influences both the scope of the analysis, whether limited to simple fault detection (FD) or extended to a complete Fault Detection, Diagnosis, and Evaluation (FDDE, and the achievable resolu-

tion in fault intensity). Specifically, the required instrumentation accuracy is strictly related to the desired evaluation step (e.g., 5%, 10%, or higher), as the measurement noise must be sufficiently lower than the thermodynamic signal shift induced by the fault to ensure a reliable diagnosis. Moreover, in experimental activities, uncertainty in sensor readings can significantly affect the calculation of key performance indicators (KPIs), which usually comes from a data reduction process, and so cannot be directly related to the uncertainty of the sensors used. For example, uncertainties in pressure and temperature measurements can strongly influence the estimation of refrigerant or secondary fluid mass flow rates, system COP, energy efficiency ratio (EER), and heat transfer rates. Otherwise, in numerical activities, sensor uncertainty can cause an improper calibration of simulation models able to simulate the system under investigation, leading to low accuracy of such models, or impair the effectiveness of FDDE processes, potentially leading to misdiagnosis.

Several studies in the literature have addressed how sensor uncertainty (for instance, of pressures and temperature) affects the experimental evaluation of heat pump performance and heating/cooling capacity. Ertesvåg [21] quantified the relative uncertainties in COP and exergy efficiency for various air-source heat pump systems, attributing them to uncertainties in temperature measurements and heat transfer calculations. Tran et al. [22] proposed a method based on intrusive measurements, specifically, refrigerant mass flow rate monitoring, for evaluating system performance, incorporating and combining the uncertainties of refrigerant and water flow rates, temperatures, pressures, densities, geometric dimensions, and thermophysical properties. Similar approaches were adopted in the IEA HPT Annex 52 project [23], which provides guidelines for propagating measurement uncertainties in the estimation of COP and heating/cooling capacity in ground-source heat pump systems. In terms of modeling uncertainty, Zhang et al. [24,25] evaluated the performance of several widely used heat pump models against manufacturer data, observing deviations in the annual average COP of up to 1.22. For refrigerant charge estimation, Kim and Braun [26] developed a virtual sensor that incorporated uncertainties in multiple temperature, pressure, and flow rate measurements.

However, to the best of the authors' knowledge, no previous studies have systematically investigated how uncertainty propagates from experimental measurements into simulation model outputs. The only partially related study is by Högberg and Vamling [27], who assessed the impact of predefined uncertainty ranges in thermodynamic and transport properties, compressor efficiency calibration laws, and correlations for heat transfer coefficients and pressure drops on COP predictions. Nonetheless, their study did not consider the influence of sensor uncertainty, such as that of temperature, pressure, and flow rate measurements, on machine-level variables and model results. Moreover, although several studies have focused on model-based FDDE, a systematic investigation of how sensor precision affects the reliability of these calibrated models is still missing in the literature. To fill these gaps, the present study was designed with the following objectives:

(1) To assess the impact of measurement uncertainties, including water mass flow rates, refrigerant and water pressures and temperatures, compressor speed, and power consumption, on key performance indicators (KPIs) such as refrigerant mass flow rate, energy efficiency ratio (EER), cooling capacity, and condenser heat load in a residential air-to-water heat pump system operating with propane in cooling mode.
(2) To investigate how these uncertainties propagate into the simulation model results, including the estimation of the required refrigerant charge. This includes additional uncertainty from the calibration of sub-models related to the compressor, heat exchangers, and void fraction correlations.

This investigation is designed as a formal pre-design phase of the experimental measurement chain. Rather than a simple preliminary step, this study provides a quantitative assessment

of how sensor uncertainty propagates through the calibration of the system's sub-models. This approach is essential to establish the instrumentation requirements and the detectability limits of the faults under investigation. By defining the trade-offs between hardware accuracy and calibration quality, this work ensures that the subsequent experimental phase, conducted on the finalized test rig, is supported by a measurement suite that guarantees consistent and acceptable uncertainty levels in both raw data and model predictions.

2. Heat Pump System Description and Modeling

2.1. Experimental Apparatus

The experimental test bench is based on a reversible air-to-water heat pump system with a nominal heating capacity of 7.80 kW, evaluated under standard conditions defined by the EN14511 regulation [28], with water and air inlet temperatures of 30 °C and 7 °C, respectively. Under these conditions, the system achieves an energy efficiency ratio (EER) of 4.40. The system is composed of a rotary compressor, a brazed plate heat exchanger (BPHX, evaporator in cooling mode), a fin-and-tube heat exchanger (FTHX, condenser in heating mode), and an electronic expansion valve (EEV), and operates with propane (R290) as the working fluid. The choice of propane as the working fluid aligns with current regulatory trends aimed at phasing out high-GWP refrigerants, promoting the adoption of natural alternatives. Among these, propane stands out as a promising option due to its favorable thermophysical and heat transfer properties [29], as well as its system efficiency [30], compared with traditional refrigerants such as CO_2, which operates at extremely high pressures, and ammonia, which presents severe toxicity risks. Despite its high flammability, which necessitates additional safety measures and potentially higher capital costs [31], propane remains a viable and increasingly adopted solution for systems in the future. The total refrigerant charge is 0.900 kg, and a charge accumulator is installed at the condenser outlet.

Although the system was originally equipped with internal sensors, a new, extensively instrumented system with additional external sensors will be installed to enable detailed monitoring of key thermodynamic variables under various operating conditions. External pressure transducers and thermocouples will be strategically placed to monitor pressures and temperatures at critical points, particularly at the compressor and expansion valve inlets and outlets. Additionally, a Coriolis-type mass flow meter will be installed on the water side of the BPHX for an accurate measurement of water mass flow rate. Water and air temperatures will be monitored using resistance temperature detectors (RTDs), whereas the compressor electrical power will be monitored by means of a wattmeter. The experimental measurements will be acquired using two Agilent 34972A data loggers, each equipped with three modules providing 20 voltage channels and two current channels. All sensor signals (temperature, pressure, flow rate, and electrical power) were recorded simultaneously with a sampling time of 5 s and stored for post-processing.

A schematic representation of the system layout, including main components and planned sensor locations, is provided in Figure 1, while photographs of the experimental heat pump are provided in Figure 2. Additional technical specifications of components and sensor specifications are listed in Table 1.

Table 1. Main components, conducted measures, and corresponding typologies.

Component/Measure	Type	Component/Measure	Sensor Type
Compressor	Rotary	Water/air/refrigerant pressure (×6)	Absolute/differential pressure transducers
Evaporator	Plate HEX	Electrical power (×3)	wattmeter

Table 1. *Cont.*

Component/Measure	Type	Component/Measure	Sensor Type
Condenser	Fin-and-tube HEX	Air mass flow rate (×1)	Measurement according to Ashrae 41.2 [32]
Expansion valve	Electronic expansion valve	Compressor/fan frequencies	Magnetic encoder
Water mass flow rate (×1)	Coriolis flow meter	Water/air/refrigerant temperatures (×8)	RTDs
Valve percentage opening	Stepper motor signal	-	-

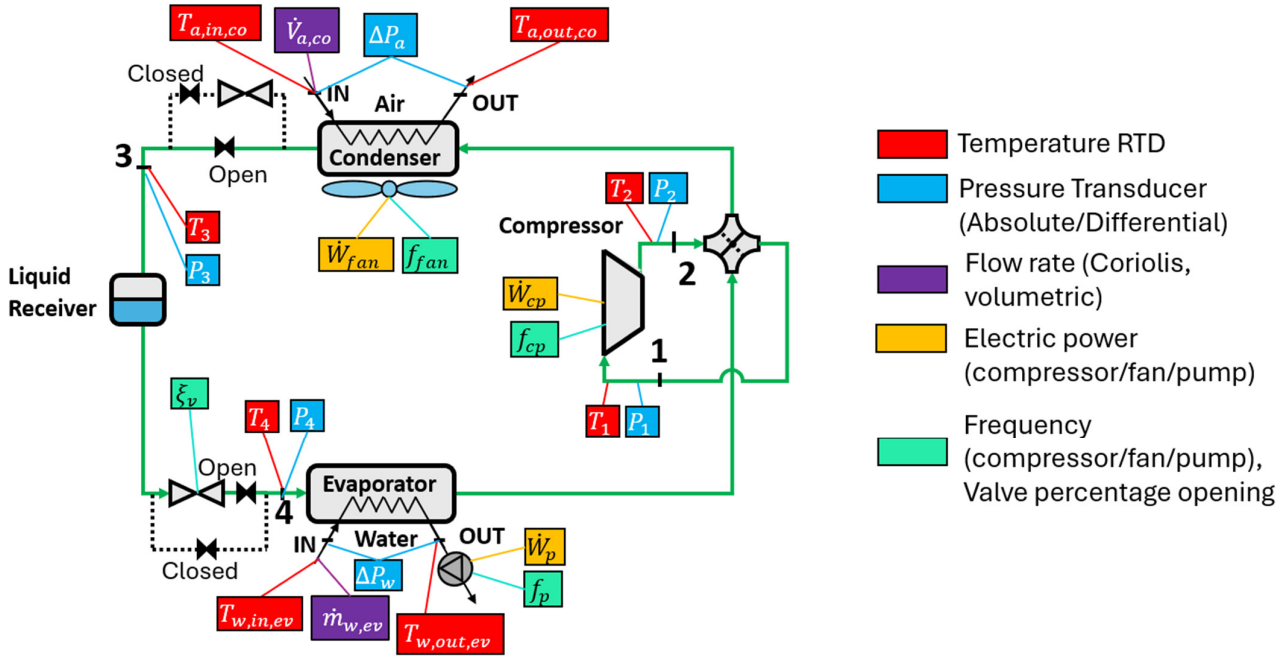
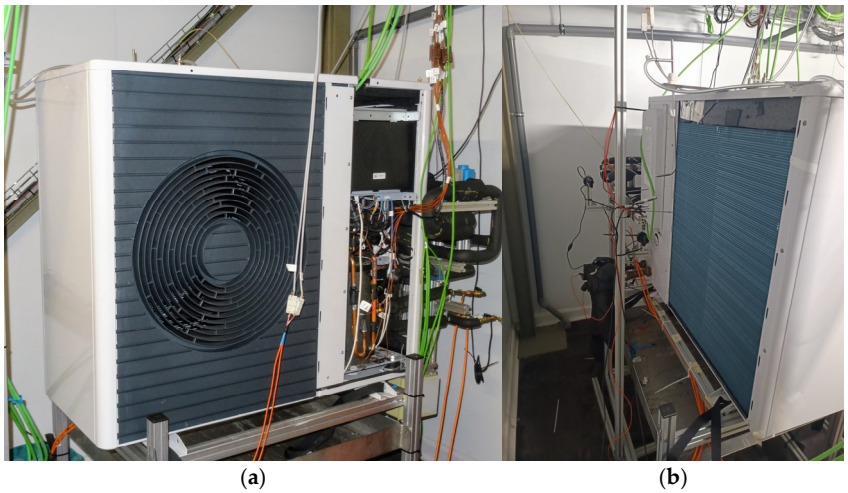


Figure 1. Schematic of the experimental apparatus piping and sensors used. Numbers refer to the thermodynamic states of the system schematic. 1: Evaporator Outlet/Compressor Inlet; 2: Compressor Outlet/Condenser Inlet; 3: Condenser Outlet/Expansion Valve Inlet; 4: Expansion Valve Outlet/Evaporator Inlet.



(**a**) (**b**)

Figure 2. Photograph of the experimental apparatus: front (**a**) and back (**b**).

2.2. System Modeling

The entire system was modeled by coupling a series of sub-models, each representing a specific component of the heat pump, including the compressor, expansion valve, tube-and-fin heat exchanger, and brazed plate heat exchanger. The simulation model is here employed as a virtual test bench. This approach allows for a controlled environment where the isolated impact of sensor accuracy can be quantified, providing a benchmark for the future experimental validation phase.

For the compressor, both the mass flow rate ($\dot{m}_{comp}$) and the overall global efficiency (η_g) were evaluated as functions of the compression pressure ratio (β_c), following the same modeling approach adopted by Mauro et al. [15]:

$$\dot{m}_{cp} = \rho_1 \cdot \frac{\dot{V}_{cp}}{3600} = \frac{\rho_1}{3600} \cdot [a \cdot \beta + b] \quad (1)$$

$$\eta_g = \frac{h_{2,is} - h_1}{h_2 - h_1} = \frac{c \cdot \beta + d}{\beta^2 + e \cdot \beta + f} \quad (2)$$

a, b, c, d, e and f are coefficients calibrated on manufacturer data by minimizing root mean squared error between experimental measurements and model prediction. The values obtained for these coefficients are reported in Table 2, for four different compressor rotational speeds, along with the coefficient of determination (R^2) related to the goodness of fit.

Table 2. Calibration coefficient used in the equations for the evaluation of the compressor mass flow rate and global efficiency, and corresponding goodness-of-fit prediction as a function of the actual rotational speed of the compressor.

n [rpm]	*a*	*b*	*c*	*d*	*e*	*f*	$R^2(\dot{V})$	$R^2(\eta_g)$
1800	−0.1032	3.2601	9.003	−9.003	8.886	−8.608	0.91	0.98
3600	−0.1757	6.6021	13.704	−13.704	15.926	−15.205	0.91	0.86
5400	−0.2322	10.0547	13.680	−13.679	15.688	−12.324	0.92	0.81
7200	−0.2862	13.6494	13.722	−13.720	16.598	−8.540	0.97	0.84

With regards to the expansion valve, the refrigerant mass flow rate ($\dot{m}_{valve}$) was modeled as a function of the inlet density (ρ_3) and the pressure drop across the valve ($P_{co} - P_{ev}$). This approach follows the methodology proposed by Yu et al. [33], using the following expression:

$$\dot{m}_{valve} = \xi_v \cdot K_v \cdot \sqrt{\rho_3 \cdot (P_{co} - P_{ev})} \quad (3)$$

where ξ_v represents the valve percentage opening, and K_v is a calibration coefficient derived from manufacturer data, equal to 0.6742×10^{-4}.

The fin-and-tube and brazed plate heat exchangers (HEXs) were modeled using a spatial integration approach. Geometrical modeling for both types is carried out following the methodology of Shah and Sekulic [34]. Conversely, with regard to heat transfer, for the fin-and-tube HEX, a two-dimensional integration was conducted. The heat transfer coefficients (HTC) for flow condensation and de-superheating were calculated using the correlations of Shah [35] and Dittus-Boelter [36], respectively. Air-side HTC and pressure drop were calculated using the correlation proposed by Wang [37]. In contrast, the plate heat exchanger was modeled using a one-dimensional approach. The flow boiling HTC was evaluated using the Amalfi–Thome correlation [38], while the water-side HTC and pressure drops were determined using the Martin correlation [39]. For both heat exchangers, refrigerant-side pressure drops were neglected.

Based on the geometrical and heat transfer characterization, an infinitesimal global conductance was calculated by accounting for all conductive and convective thermal resistances, as follows:

$$UdA = \left(dR_{c,ref} + dR_k + dR_{c,w}\right)^{-1} \quad (4)$$

Therefore, the thermal power exchanged by each infinitesimal element of the heat exchanger was calculated using the ε-NTU method [40]. To simulate the overall behavior of the heat exchanger, an iterative procedure was implemented on the secondary fluid temperature profile to achieve convergence between the calculated heat transfer and the target heating or cooling load.

Finally, regarding the refrigerant charge, it was estimated as the sum of the contributions from each component and piping section. Single-phase contributions (m_{sp}) such as those in the liquid line, compressor suction, and discharge lines, were calculated based on refrigerant density (ρ) under specific test conditions and the corresponding pipe volume, using the following equation:

$$m_{sp} = \rho \cdot S \cdot L \quad (5)$$

Conversely, the two-phase contributions (m_{tp}) corresponding to the condensing and evaporating sections of the heat exchangers were evaluated as a function of the liquid (ρ_L) and vapor (ρ_V) densities, as follows, averaged by means of the void fraction (α), evaluated with the Rouhani–Axelsson correlation [41].

$$dm_{tp} = [\rho_L \cdot (1 - \alpha) + \rho_V \cdot \alpha] \cdot S \cdot dL \quad (6)$$

The entire model was implemented in MATLAB R2024b [42], using Refprop 10 [43] for the evaluation of thermodynamic properties.

A flow chart showing the computational procedure of the model is reported in Figure 3. In detail, firstly, values for the condensing and user temperature (T_{co}, T_{user}) were chosen, as well as a saturated liquid condition at the inlet of the expansion valve ($x_3 = 0$), which is guaranteed by the presence of the liquid receiver [44]. At the beginning, the valve was considered fully open ($\xi_v = 1$) and, with that, an iterative procedure on the evaporating temperature (T_{ev}) was adopted in order to have the same refrigerant mass flow rate at both the compressor (evaluated with Equation (1)) and the valve (evaluated with Equation (3)). A first attempt value for the evaporator superheating (ΔT_{sh}) was fixed, and using that value, the compressor global efficiency (Equation (2)), and all corresponding thermodynamic states (1, 2, 3, 4) were evaluated. In detail, state 1 (outlet evaporator) was evaluated using evaporating pressure (P_{ev}) and superheat (ΔT_{sh}); state 2 (outlet compressor) using condensing pressure (P_{co}), the compressor outlet isentropic state (2 s), and the global efficiency definition (η_g, Equation (2)); state 3 (condenser outlet) as saturated liquid ($x = 0$) at the condensing pressure (P_{co}); and state 4 (expansion valve outlet) using an isenthalpic process across the expansion valve ($h_4 = h_3$) at the evaporating pressure (P_{ev}). Therefore, the evaporator superheating was iterated to find a thermal power convergence between first principles and heat transfer (Equation (4) and $\varepsilon-$ NTU method), inside the evaporator (BPHE), and thermodynamic states are re-evaluated. A further iteration was also conducted on the valve opening percentage, in order to have evaporator ΔT_{sh} convergence results exactly equal to a predefined value (which was fixed to 10 °C). Finally, a similar iterative procedure was conducted on the condenser.

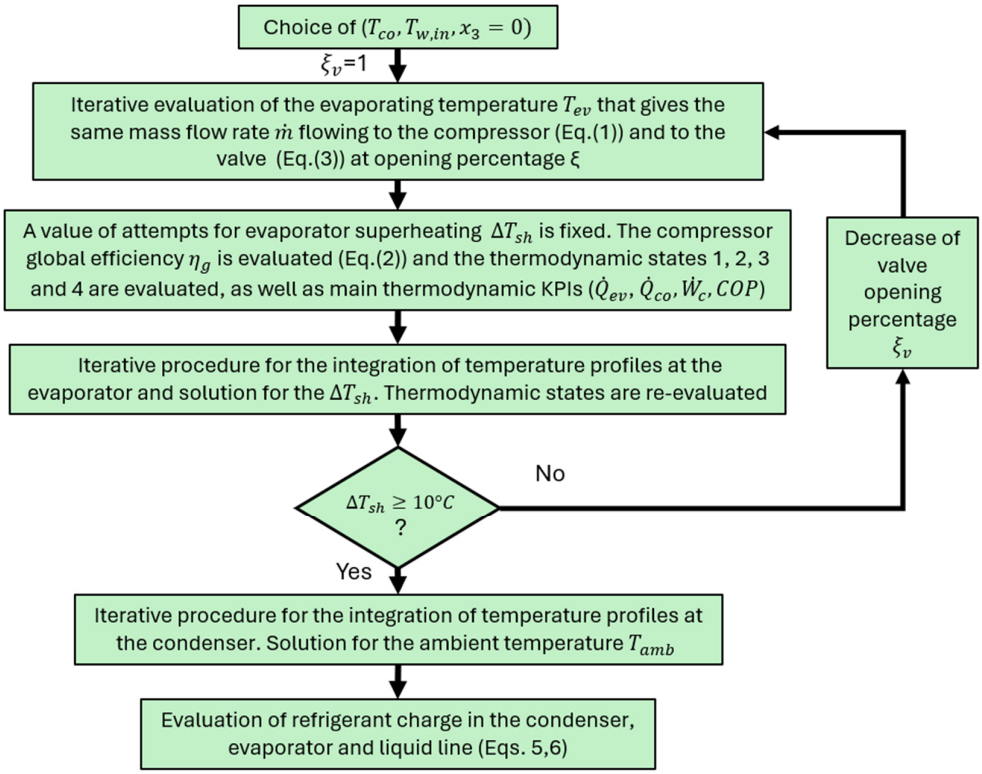


Figure 3. Flow chart of the resolution steps to follow to couple all the sub-models and simulate the entire system.

The modeling methodology adopted in this study relies on well-established and widely validated approaches for individual component modeling used by numerous research groups [45,46]. However, since this work represents a preliminary analysis aimed at defining the required sensor accuracy for the experimental setup, a comprehensive validation of the complete machine model will be carried out in future studies, once the test facility is fully finalized.

3. Methodology: Uncertainty Analysis and Experimental Data Reduction

The investigation presented in this paper is structured into several phases, as illustrated in the graphical abstract reported in Figure 4. First, a virtual experimental test was performed using the simulation model to replicate the operation of the experimental setup (Step 1). Subsequently, two different sensor configurations were considered, each characterized by distinct levels of measurement accuracy (Step 2), as detailed in Section 3.1. For both configurations, and assuming a specific experimental data reduction process described in Section 3.2, the propagation of measurement uncertainties on key performance indicators (KPIs) was evaluated (Step 3a), leading to the estimation of uncertainties for EER, cooling capacity, condenser heat load, and refrigerant mass flow rate (Step 3b). These experimental uncertainties were then combined with modeling-related uncertainties, namely those arising from compressor calibration curves, heat transfer coefficient (HTC) correlations, and void fraction models (Step 4a), also described in Section 3.1, and incorporated into the simulation model inputs (Step 4b), as detailed in Section 3.3. This allowed for the quantification of output uncertainties from the simulation model (Step 4c). Finally, the uncertainty levels originating from experimental measurements and those derived from the simulation model were compared (Step 5).

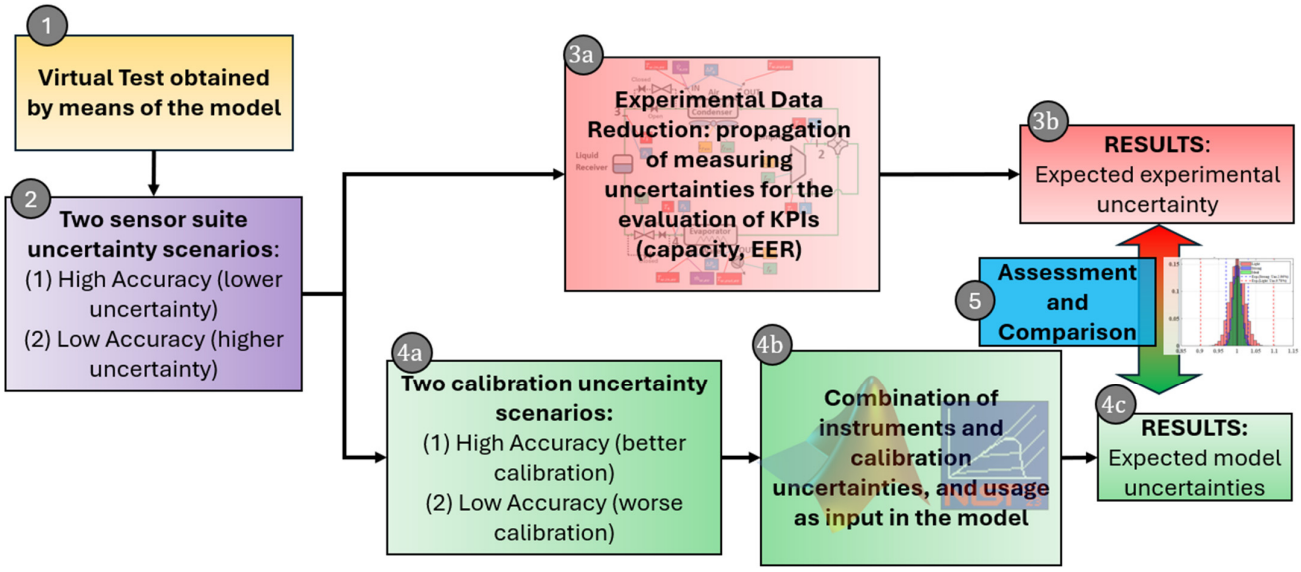


Figure 4. Graphical abstract reporting a summary of the methodology employed in this work.

3.1. Measuring Instruments and Model Calibration Uncertainty

As previously outlined in Section 2.1, the heat pump system is equipped with various sensors, including pressure transducers, temperature probes, mass flow meters, and power meters. A wide range of sensors is available on the market, differing in terms of performance, cost, and associated measurement uncertainty. To reflect this variability, two sensor accuracy scenarios were considered in this study: a "high-accuracy" scenario, based on high-end, laboratory-grade instruments with low measurement uncertainty, and a "low-accuracy" scenario, based on more affordable, commercially available sensors characterized by higher uncertainty. A summary of the assumed measurement uncertainties for both scenarios is reported in Table 3. These levels for both scenarios were selected based on the findings of our previous work [20]. Both sensor suites are technically capable of supporting a full FDDE process, as they provide sufficient resolution to distinguish thermodynamic cycle shifts associated with fault intensity steps of at least 10%. Although the 'Low Accuracy' scenario reflects typical on-field monitoring constraints, the 'High Accuracy' suite is used to evaluate the feasibility of finer diagnoses (e.g., 5% steps), where the margin between measurement noise and fault signal is reduced.

Table 3. Experimental uncertainty values used for both high- and low-accuracy scenarios.

Sensor Error	High Accuracy	Low Accuracy
Water mass flow rate	±0.21%	±0.50%
Air volumetric flow rate	±5.0%	±5.0%
Refrigerant temperature	±0.5 °C	±0.8 °C
Refrigerant pressure	±1.0%	±2.0%
Air/water temperature	±0.06 °C	±0.20 °C
Compressor speed	±1.0%	±2.0%
Compressor power consumption	±0.5%	±2.0%

The models and sub-models described in Section 2.2 are typically calibrated using experimental data. According to uncertainty propagation principles, the uncertainty associated with the calibration of these models is directly influenced by the measurement uncertainty of the sensors employed during data acquisition. Utilizing high-precision sensors (high-accuracy scenario) leads to reduced uncertainty in model calibration, while relying on lower-grade sensors (low-accuracy scenario) results in increased model un-

certainty. Accordingly, two calibration scenarios, "high accuracy" and "low accuracy", were considered in this study. The corresponding uncertainty values obtained for each sub-model calibration are summarized in Table 4.

Table 4. Calibration uncertainty values used for both low- and high-accuracy scenarios.

Calibration Error	High Accuracy	Low Accuracy
Compressor mass flow rate	±2.5%	±5.0%
Compressor global efficiency	±2.5%	±5.0%
Valve mass flow rate	±2.5%	±5.0%
Heat transfer coefficients	±5.0%	±10.0%
Void fraction	±5.0%	±10.0%

3.2. Experimental Data Reduction and Uncertainty Propagation

To simulate a virtual experimental campaign, a data reduction was applied to the measurements collected from the apparatus in order to obtain the main key performance indicators (KPIs) for the system under investigation. In particular, in this work, starting from the direct measurements obtained from the sensors shown in Figure 1, the following parameters were derived using the corresponding equations:

- Cooling capacity ($\dot{Q}_{ev}$):

$$\dot{Q}_{ev} = \dot{m}_w \cdot c_w \cdot (T_{w,in,ev} - T_{w,out,ev}) \tag{7}$$

where $\dot{m}_w$ is the water mass flow rate, c_w is the water specific heat, and $T_{w,in,ev}$ and $T_{w,out,ev}$ are water inlet and outlet temperatures, respectively;

- Heating capacity ($\dot{Q}_{co}$):

$$\dot{Q}_{co} = \dot{m}_a \cdot c_a \cdot (T_{a,out,co} - T_{a,in,co}) \tag{8}$$

where $\dot{m}_a$ is the air mass flow rate, c_a is the air specific heat, and $T_{a,out,co}$ and $T_{a,in,co}$ are air outlet and inlet temperatures, respectively;

- Refrigerant mass flow rate ($\dot{m}_{ref}$):

$$\dot{m}_{ref} = \dot{Q}_{ev} / (h_1 - h_4) \tag{9}$$

where $\dot{Q}_{ev}$ is the cooling capacity, h_1 is the refrigerant enthalpy at the outlet of the evaporator, and h_4 is the refrigerant enthalpy at evaporator inlet;

- Energy efficiency ratio (EER):

$$EER = \dot{Q}_{ev} / \dot{W}_{cp} \tag{10}$$

where $\dot{W}_{cp}$ is compressor power consumption. The uncertainty (u) for each of the previously calculated quantities is determined using the law of uncertainty propagation [47], expressed as:

$$u(z) = \sqrt{\left(\frac{\partial f}{\partial x} u(x)\right)^2 + \left(\frac{\partial f}{\partial y} u(y)\right)^2 + \cdots} \tag{11}$$

where δz is the total uncertainty of the function f, $\frac{\partial f}{\partial x}$ and $\frac{\partial f}{\partial y}$ are the partial derivatives of f with respect to each measured variable. $u(x)$ and $u(y)$ represent the experimental uncertainty of the respective measured value. Equations for each of the derived variables from the data reduction are reported in Appendix A.

3.3. Virtual Test and Numerical Methodology

To perform the uncertainty analysis, a virtual test was carried out using the developed models. The input variables for the virtual test were as follows: condenser air inlet temperature (35 °C), evaporator water inlet temperature (13 °C), compressor speed (2500 rpm), valve inlet vapor quality (0), target evaporator superheating (10 °C), condenser air mass flow rate (0.3 kg/s), evaporator water mass flow rate (0.222 kg/s), and the geometrical characteristics of the piping, heat exchangers, compressor, and valve, which were measured directly from the real prototype. The output variables from the virtual test, particularly those needed for the calculation of the KPIs, will be discussed in the next section.

Each input variable was represented as an array spanning an interval defined by its nominal value plus and minus its uncertainty. This interval was discretized using non-uniform spacing: the spacing was broader at the extremes and denser near the center of the interval. This approach allowed the distribution of values to approximate a Gaussian distribution centered around the nominal value. An example of input variable uncertainty is shown in Figure 5a for the compressor mass flow rate in the low-accuracy scenario ($u(\dot{m}) = 5.0\%$) and Figure 5b for the compressor global efficiency in the high-accuracy scenario ($u(\eta_g) = 5.0\%$).

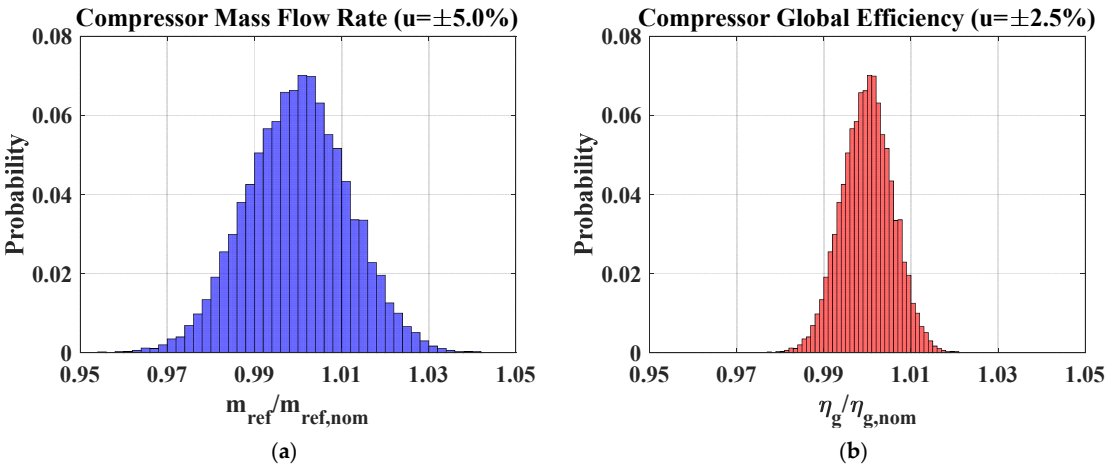


Figure 5. Gaussian distribution of the compressor mass flow rate calibration in the low-accuracy scenario (**a**) and the compressor global efficiency in the high-accuracy scenario (**b**), used as an input variable of the model.

A brute-force approach involving an exhaustive search of all possible parameter combinations was discarded due to the excessive computational burden. Subsequently, a Monte Carlo method with Latin Hypercube Sampling (LHS) [48] was adopted. Compared with standard sampling, LHS ensures a more uniform coverage of the input domain by partitioning the probability distributions into intervals of equal probability, significantly reducing the number of simulations required to achieve statistical convergence. For each scenario investigated ("high accuracy" and "low accuracy"), 20,000 combinations were generated. Additionally, an "ideal" scenario consisting of 20,000 further combinations was simulated to isolate model-related uncertainties from instrumental ones. The sample size of 20,000 was determined through a preliminary convergence study, which showed that mean values and standard deviations reach statistical stability beyond these values. Each set of 20,000 simulations required approximately 12 h of computational time, resulting in a total of 36 h to complete the entire uncertainty analysis for the three scenarios.

4. Results

4.1. Experimental Uncertainty

The virtual experiment, carried out using the numerical model described in Section 3.3, produced the following output variables under the input conditions specified above: evaporator temperature of −3.3 °C (corresponding to an evaporating pressure of 4.29 bar), condenser temperature of 51.6 °C (condensing pressure of 17.75 bar), condenser air outlet temperature of 46.6 °C, evaporator water outlet temperature of 10.4 °C, and evaporator superheating of 10.0 K. A complete summary of the virtual test results is provided in Table 5.

Table 5. Output variables and values of the virtual experiment.

Output Variable	Value
Evaporating temperature	−3.3 °C
Evaporating pressure	4.29 bar
Condensing temperature	51.6 °C
Condensing pressure	17.8 bar
Condenser air outlet temperature	46.6 °C
Evaporator water outlet temperature	10.4 °C
Superheating	10 K
Compressor outlet temperature	84.8 °C
Valve opening percentage	19.2%
Refrigerant mass flow rate	0.0100 kg/s
Cooling capacity	2.46 kW
Heating capacity	3.57 kW
Compressor power consumption	1.12 kW
EER	2.20
Refrigerant charge	498 g

These results provide a comprehensive overview of the heat pump system's performance under nominal conditions. The next step involved incorporating the effect of input uncertainty around these nominal conditions. Measurement uncertainties were propagated to the KPIs, including EER, cooling capacity, condenser heat load, and refrigerant mass flow rate, using the uncertainty propagation method described in Equation (11). The resulting uncertainties for these KPIs are reported in Table 6. Specifically, for the cooling capacity, calculated using Equation (7), the uncertainty was 2.93% in the high-accuracy scenario and 9.77% in the low-accuracy scenario. For the heating capacity, the achieved uncertainties were 5.05% and 5.50% in the high- and low-accuracy scenarios, respectively. The EER showed an uncertainty of 2.98% in the high-accuracy case and 9.97% in the low-accuracy case, while for the refrigerant mass flow rate, the uncertainties were 2.96% and 9.78%, respectively. Overall, these results indicate that the high-accuracy scenario consistently yields uncertainties below 3–4% for all variables, except for heating capacity, which is notably affected by the uncertainty in the air mass flow rate. In contrast, the low-accuracy scenario resulted in higher uncertainties, generally ranging from 6% to 10%. These findings align with the experimental investigation by Ertesvåg [21], who reported COP uncertainties between 5% and 9%, depending on the climatic conditions analyzed and assuming similar sensor accuracy. Similarly, Kim and Braun [26] reported uncertainties of 1% for cooling capacity and 3.5% for COP, using slightly more accurate instrumentation than in the present study.

Table 6. Experimental uncertainties results: high- and low-accuracy scenarios.

Experimental Uncertainty	High Accuracy	Low Accuracy
Cooling capacity	2.93%	9.77%
Condenser heat load	5.05%	5.50%

Table 6. *Cont.*

Experimental Uncertainty	High Accuracy	Low Accuracy
EER	2.98%	9.97%
Refrigerant mass flow rate	2.96%	9.78%

4.2. Projection of the Experimental Uncertainty on Model Outputs

In this section, uncertainties are quantified by simulating 20,000 input combinations for each scenario ('high accuracy', 'low accuracy', and 'ideal'), with input values sampled via LHS from Gaussian distributions. The results of these three simulations are presented in the histogram plots shown in Figure 6. These plots illustrate the variability of the main output parameters: evaporator pressure (Figure 6a), refrigerant mass flow rate (Figure 6b), cooling capacity (Figure 6c), compressor power consumption (Figure 6d), EER (Figure 6e), and refrigerant charge (Figure 6f). Additionally, two vertical dashed lines, representing the projected uncertainty bounds for both accuracy scenarios, as defined in Section 3.1, are included in each plot. The green bars correspond to the 'ideal' scenario, the purple bars to the 'high accuracy' scenario, and the pink bars to the 'low accuracy' scenario.

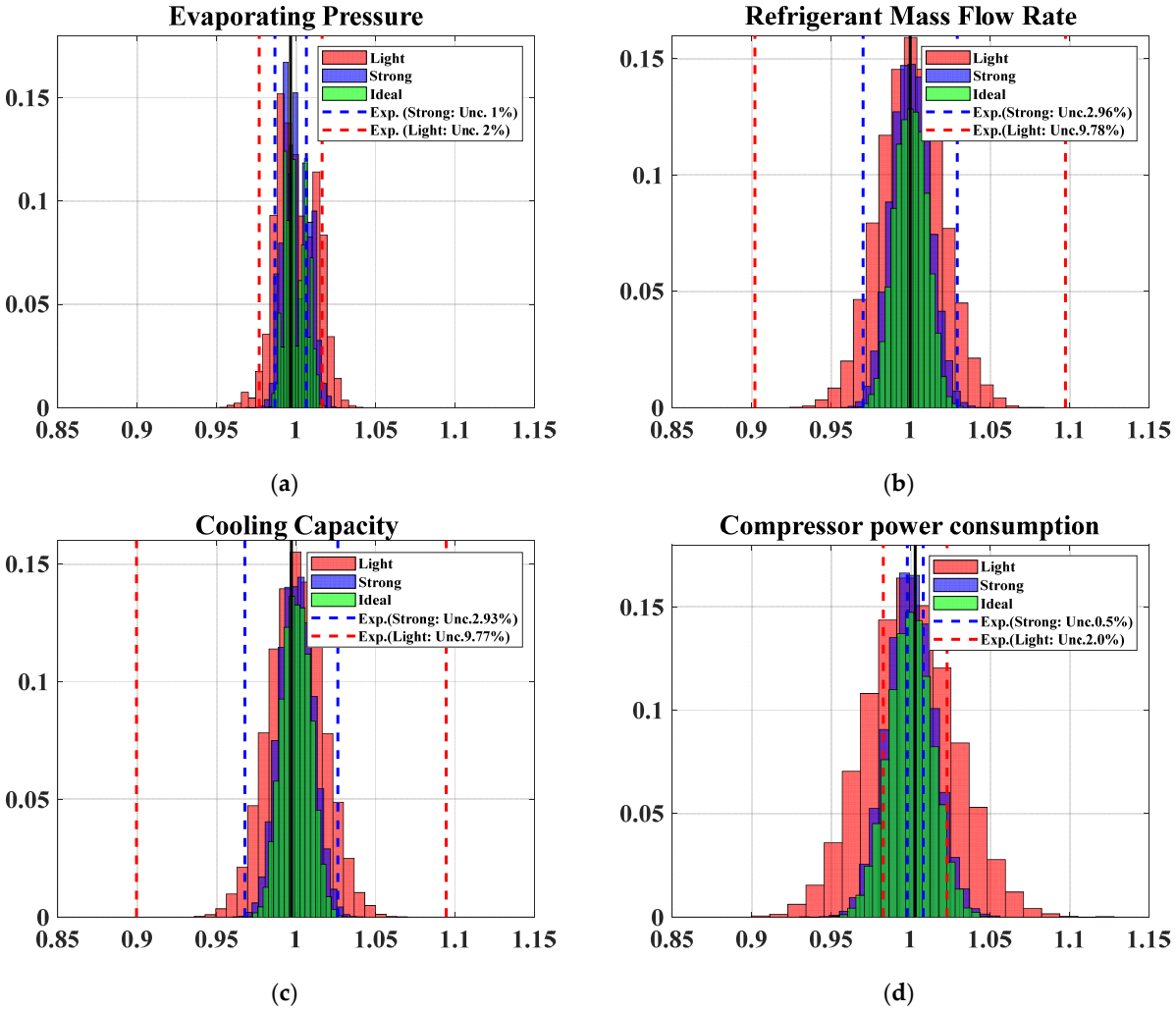


Figure 6. *Cont.*

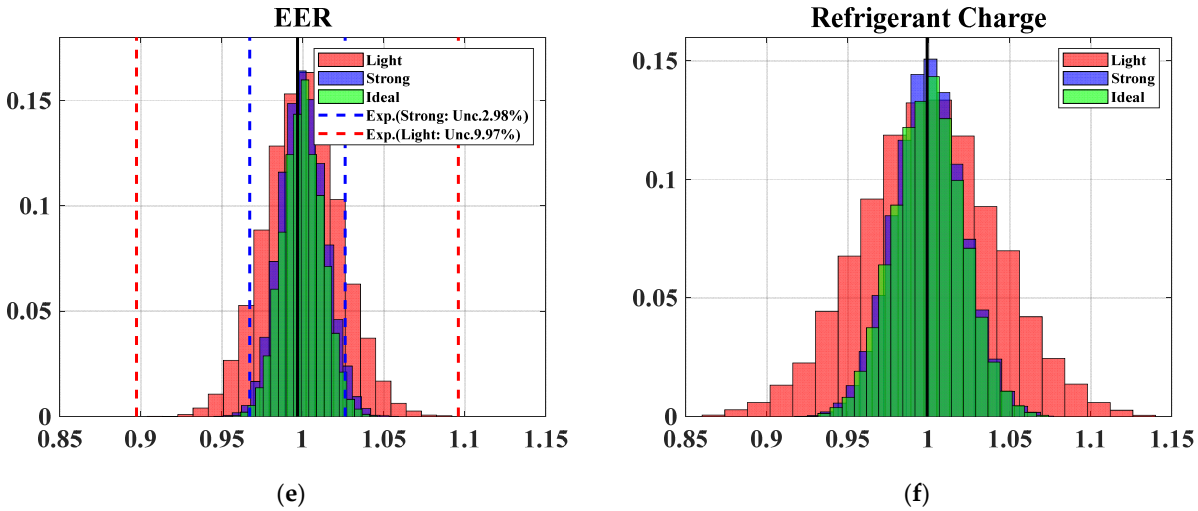


Figure 6. Normalized uncertainties propagation to the model outputs: (**a**) evaporating pressure; (**b**) refrigerant mass flow rate; (**c**) cooling capacity; (**d**) compressor power consumption; (**e**) EER; (**f**) refrigerant charge. The black line refers to the expected experimental value.

It is worth noting that, for certain variables, such as cooling capacity, refrigerant mass flow rate, and EER, model uncertainty is lower than the corresponding experimental uncertainty, particularly in the low-accuracy scenario. Conversely, for other variables, the uncertainties are generally comparable (e.g., evaporating pressure), or in some cases, the model introduces higher uncertainty due to the propagation of input variability, as observed for compressor power consumption. Overall, in the high-accuracy scenario, model uncertainty remains within $\pm 2\%$ for pressures and $\pm 5\%$ for refrigerant mass flow rate, cooling capacity, and EER. In the low-accuracy scenario, these ranges increase to approximately $\pm 5\%$ for pressures and up to $\pm 10\%$ for the other quantities. Regarding refrigerant charge, the uncertainty is approximately $\pm 7\%$ in the high-accuracy scenario and can reach nearly $\pm 15\%$ under low-accuracy conditions.

These findings highlight the critical role of instrumentation accuracy, particularly in the estimation of refrigerant charge. However, the influence of sub-model calibration uncertainty should also be carefully considered, as it contributes non-negligibly to the overall uncertainty.

5. Conclusions

This study investigated the impact of experimental uncertainty and model calibration errors on the reliability of numerical simulation results for a residential air-to-water heat pump system operating in cooling mode with R290, both in the presence and absence of soft faults. Conducted within the framework of the BEYOND project, the analysis assessed how these uncertainties propagate to key performance indicators (KPIs) and refrigerant charge predictions.

The main findings are summarized as follows:

- Effective fault detection and diagnostics (FDDE) must consider uncertainties in both measurements and model calibration, as these factors can significantly compromise the reliability of FDDE tools and algorithms. Two levels of instrumentation uncertainty were considered: a “low accuracy” scenario (based on commercially available sensors) and a “high accuracy” scenario (using laboratory-grade instrumentation).
- Following experimental data reduction, uncertainties in several derived quantities, such as cooling capacity, condenser heat load, EER, and refrigerant mass flow rate, were quantified. In the “low accuracy” scenario, uncertainties exceeded 10% in some

cases, while in the "high accuracy" scenario, they remained below 3.60%. Specifically, in the low-accuracy case, uncertainties were 9.77% for cooling capacity, 5.50% for heating capacity, 9.97% for EER, and 9.78% for refrigerant charge. In the high-accuracy scenario, the corresponding values were: 2.93%, 5.05%, 2.98%, and 2.96%, respectively.

- Error propagation within the simulation model showed that, particularly in the low-accuracy scenario, model-based uncertainties were generally lower than experimental ones for variables such as refrigerant mass flow rate, cooling capacity, and EER. However, other variables, such as evaporating pressure and compressor power consumption, were more affected by uncertainty introduced through the modeling process. Overall, projected uncertainties ranged from $\pm 2\%$ to $\pm 5\%$ in the high-accuracy scenario and from $\pm 5\%$ to $\pm 10\%$ in the low-accuracy scenario.
- Finally, regarding refrigerant charge estimation, uncertainties of $\pm 7\%$ and $\pm 15\%$ were observed in the high- and low-accuracy scenarios, respectively. This highlights the importance of selecting appropriate sensor accuracy and ensuring proper model calibration to reliably predict refrigerant charge.

The methodology presented in this work provides a valuable framework for researchers to balance instrumentation accuracy and model calibration quality, potentially avoiding unnecessary costs associated with high-end sensors. In this regard, it should be noted that an extensive experimental campaign, along with the subsequent validation and detailed assessment of the model, will be performed only once the sensor suite and the testing facility are finalized, as this study intentionally serves as a preliminary design phase. Future developments may also include extending the analysis to heating mode operation, investigating different system configurations, and exploring alternative virtual test conditions.

Author Contributions: Conceptualization, F.P., L.V., and A.W.M.; methodology, L.V., E.N.-P., and A.W.M.; software, R.C.; validation, R.C., A.F.P., and B.L.-M.; formal analysis, A.F.P.; investigation, F.P. and L.V.; resources, B.L.-M. and E.N.-P.; data curation, R.C. and B.L.-M.; writing—original draft preparation, R.C. and A.F.P.; writing—review and editing, F.P., L.V., and A.W.M.; visualization, R.C.; supervision, A.W.M. and E.N.-P.; project administration, A.W.M.; funding acquisition, L.V. and A.W.M. All authors have read and agreed to the published version of the manuscript.

Funding: This research was funded by the European Innovation Council (EIC) under the project "method for smart and affordaBle Evaluation of simultaneous faults in heating and cooling sYstems based ON compresseD vapor technology" (BEYOND), Grant Agreement ID 101162436, within the European Union's Horizon Europe programme. This work was also supported by the Italian Ministry of University and Research (MUR) through the PRIN 2022 PNRR project "Vapor compression systems for heating and cooling: virtual experiments for the assessment of different types of methods for the fault detection and diagnosis and to forecast the environmental and energetic performance" (Grant No. P2022XWYYF, CUP E53D23017570001), funded by the European Union—NextGenerationEU.

Data Availability Statement: Dataset available on request from the authors. The raw data supporting the conclusions of this article will be made available by the authors on request.

Conflicts of Interest: The authors declare no conflicts of interest.

Abbreviations

The following abbreviations are used in this manuscript:

COP	Coefficient of performance [-]
EER	Energy efficiency ratio [-]
EEV	Electronic Expansion Valve
FDDE	Fault detection, diagnosis, and evaluation

HTC	Heat Transfer Coefficient [W/m^{2}K]
KPI	Key performance indicator
LHS	Latin hypercubic sampling
RTD	Resistance temperature detector
VRV/VRF	Variable refrigerant volume/variable refrigerant flow

Nomenclature

The following symbols are used in this manuscript:

Roman		Subscript	
A	Heat transfer surface [m^2]	a	Air
a, b, c, d, e, f	Compressor calibration coefficient [-]	c	Convective
c	Specific heat [J/kgK]	co	Condenser
dR	Infinitesimal thermal resistance [K/W]	cp	Compressor
h	Specific Enthalpy [J/kg]	ev	Evaporator
K_v	Valve calibration coefficient [-]	in	Inlet
L	Length [m]	is	Isentropic
n	Compressor Rotational Speed [rpm]	k	Conductive
m	Refrigerant charge [kg]	L	Liquid
$\dot{m}$	Mass flow rate [kg/s]	nom	Nominal
P	Pressure [bar]	out	Outlet
$\dot{Q}$	Thermal Power [W]	p	Pump
S	Cross-section surface [m^2]	ref	Refrigerant
T	Temperature [°C]	sp	Single phase
u	Uncertainty [-]	tp	Two-phases
U	Heat transfer conductance [W/m^{2}K]	V	Vapor
$\dot{V}$	Volumetric Flow Rate [m^3/h]	w	Water
$\dot{W}$	Electric Power [W]	1	Compressor inlet
x	Vapor quality [-]	2	Compressor outlet
		3	Valve inlet
Greek		4	Valve outlet
α	Volumetric Void Fraction [-]		
β	Compression Ratio [-]		
Δ	Variation		
ξ_v	Valve percentage opening [-]		
η_g	Compressor Global Efficiency [-]		
ρ	Density [kg/m^3]		

Appendix A. Equation for the Experimental Uncertainty Evaluations of Parameters Deriving from the Data Reduction

Here are reported the equations obtained by implementing the uncertainty propagation law (Equation (11)) for each variable derived from the data reduction. For the cooling ($\dot{Q}_{ev}$) and heating ($\dot{Q}_{co}$) capacities:

$$u\left(\dot{Q}_{ev}\right) = \sqrt{\left[c_{p,w}\cdot\left(T_{w,in,ev} - T_{w.out,ev}\right)\cdot u\left(\dot{m}_w\right)\right]^2 + 2\cdot\left[\dot{m}_w\cdot c_w\cdot u(T)\right]^2} \quad \text{(A1)}$$

$$u\left(\dot{Q}_{co}\right) = \sqrt{\left[c_{p,a}\cdot\left(T_{a,out,co} - T_{a.in,co}\right)\cdot u\left(\dot{m}_a\right)\right]^2 + 2\cdot\left[\dot{m}_a\cdot c_a\cdot u(T)\right]^2} \quad \text{(A2)}$$

For the enthalpies of the thermodynamic cycle states, the following expressions were used:

$$u(h_1) = \sqrt{\left[\frac{dh_1}{dP}\cdot u(P_{co})\right]^2 + \left[\frac{dh_1}{dT}\cdot u\left(T_{ref}\right)\right]^2} \quad \text{(A3)}$$

$$u(h_2) = \sqrt{\left[\frac{dh_2}{dP}\cdot u(P_{ev})\right]^2 + \left[\frac{dh_2}{dT}\cdot u\left(T_{ref}\right)\right]^2} \tag{A4}$$

$$u(h_3) = u(h_4) = \left[\frac{dh_3}{dP}\cdot u(P_{co})\right] \tag{A5}$$

The partial derivatives of enthalpies were obtained through Refprop 10 [43] using the following inputs:

$$\frac{dh_1}{dP} = \frac{h(T_1, P_{ev} - u(P_{ev})) - h(T_1, P_{ev} + u(P_{ev}))}{2\cdot u(P_{ev})} \tag{A6}$$

$$\frac{dh_2}{dP} = \frac{h(T_2, P_{co} - u(P_{co})) - h(T_2, P_{co} + u(P_{co}))}{2\cdot u(P_{co})} \tag{A7}$$

$$\frac{dh_3}{dP} = \frac{h(x = 0, P_{co} - u(P_{co})) - h(x = 0, P_{co} + u(P_{co}))}{2\cdot u(P_{co})} \tag{A8}$$

$$\frac{dh_1}{dT} = \frac{h(T_1 - u(T_{ref}), P_{ev}) - h(T_1 + u(T_{ref}), P_{ev})}{2\cdot u(T_{ref})} \tag{A9}$$

$$\frac{dh_2}{dT} = \frac{h(T_2 - u(T_{ref}), P_{co}) - h(T_2 + u(T_{ref}), P_{co})}{2\cdot u(T_{ref})} \tag{A10}$$

Finally, experimental uncertainty for the refrigerant mass flow rate and the EER were evaluated as follows:

$$u(\dot{m}_{ref}) = \sqrt{\left[\frac{1}{h_1 - h_4}\cdot u(\dot{Q}_{ev})\right]^2 + \left[\frac{\dot{Q}_{ev}}{(h_1 - h_4)^2}\cdot u(h_1)\right]^2 + \left[-\frac{\dot{Q}_{ev}}{(h_1 - h_4)^2}\cdot u(h_4)\right]^2} \tag{A11}$$

$$u(EER) = \sqrt{\left[\frac{1}{\dot{W}_{cp}}\cdot u(\dot{Q}_{ev})\right]^2 + \left[-\frac{\dot{Q}_{ev}}{\dot{W}_{cp}^2}\cdot u(\dot{W}_{cp})\right]^2} \tag{A12}$$

References

1. Buildings, Energy Systems. Available online: https://www.iea.org/energy-system/buildings (accessed on 13 February 2026).
2. Morte, I.B.B.; de Queiroz, F.A.O.; Morgado, C.R.; de Medeiros, J.L. Electrification and Decarbonization: A Critical Review of Interconnected Sectors, Policies and Sustainable Development Goals. *Energy Storage Sav.* **2023**, *2*, 615–630. [CrossRef]
3. The European Parliament; The Council of the European Union. *Regulation (EU) 2024/573 of the European Parliament and of the Council of 7 February 2024 on Fluorinated Greenhouse Gases, Amending Directive (EU) 2019/1937 and Repealing Regulation (EU)*; No. 517/2014; Publications Office of the European Union: Luxembourg, 2024.
4. Commission Regulation (EU) 2016/2281. 30 November 2016. Available online: https://eur-lex.europa.eu/legal-content/en/TXT/?uri=CELEX:32016R2281 (accessed on 10 March 2026).
5. Rossi, T.M.; Braun, J.E. A Statistical, Rule-Based Fault Detection and Diagnostic Method for Vapor Compression Air Conditioners. *HVACR Res.* **1997**, *3*, 19–37. [CrossRef]
6. Domanski, P.A.; Henderson, H.I.; Payne, W.V. *Sensitivity Analysis of Installation Faults on Heat Pump Performance*; US Department of Commerce, National Institute of Standards and Technology: Gaithersburg, MD, USA, 2014. Available online: https://nvlpubs.nist.gov/nistpubs/TechnicalNotes/NIST.TN.1848.pdf (accessed on 10 February 2026).
7. Comstock, M.C.; Braun, J.E.; Groll, E.A. The sensitivity of Chiller Performance to Common Faults. *HVAC&R Res.* **2001**, *7*, 263–279. [CrossRef]
8. Comstock, M.C.; Braun, J.E. *Development of Analysis Tools for the Evaluation of Fault Detection and Diagnostics in Chillers; ASHRAE Research Project 1043-RP; also Ray W. Herrick Laboratories*; Purdue University: West Lafayette, IN, USA, 1999.
9. Bellanco, I.; Belío, F.; Vallés, M.; Gerber, R.; Salom, J. Common fault effects on a natural refrigerant, variable-speed heat pump. *Int. J. Refrig.* **2022**, *133*, 259–266. [CrossRef]

10. Noel, D.; Riviere, P.; Teuillieres, C.; Cauret, O.; Marchio, D. Experimental Characterization of Fault Impacts on the Functioning Variables of an Inverter Driven Heat Pump. In Proceedings of the 10th International Conference on System Simulation in Buildings, Liège, Belgium, 10–12 December 2018.
11. Gou, W.; Ren, Z.; Chen, H.; Xing, L.; Zhou, Z.; Xia, X.; Shi, J. Experimental research on the performance and parameters sensitivity analysis of variable refrigerant flow system with common faults imposed in heating mode. *Energy Build.* **2023**, *278*, 112624. [CrossRef]
12. Zhou, Z.; Wang, J.; Chen, H.; Wei, W.; Xu, C. An online compressor liquid floodback fault diagnosis method for variable refrigerant flow air conditioning system. *Int. J. Refrig.* **2020**, *111*, 9–19. [CrossRef]
13. Guo, Y.; Du, C.; Liu, X.; Zhang, X.; Jin, Z. Research on attention-based fault diagnosis and multi-parameter joint optimization of CO_2 heat pump system. *Appl. Therm. Eng.* **2026**, *289*, 129942. [CrossRef]
14. Li, W.; Sui, W.; Cheng, L.; Ji, Y.; Guo, Y.; Zhu, J. Quantifying seasonal demand-side flexibility in residential air conditioning under diverse control strategies. *Energy Build.* **2025**, *352*, 116764. [CrossRef]
15. Mauro, A.W.; Pelella, F.; Viscito, L. Performance degradation of air source heat pumps under faulty conditions. *Case Stud. Therm. Eng.* **2023**, *45*, 103010. [CrossRef]
16. Llopis-Mengual, B.; Navarro-Peris, E. Effects of simultaneous soft faults in a reversible and variable-speed air-to-water heat pump. *Appl. Therm. Eng.* **2024**, *254*, 123883. [CrossRef]
17. Hu, Y.; Yuill, D.P. Effects of multiple simultaneous faults on characteristic fault detection features of a heat pump in cooling mode. *Energy Build.* **2021**, *251*, 111355. [CrossRef]
18. Hu, Y.; Yuill, D.P. Multiple simultaneous faults' impacts on air-conditioner behavior and performance of a charge diagnostic method. *Appl. Therm. Eng.* **2022**, *215*, 119015. [CrossRef]
19. Mauro, A.W.; Pelella, F.; Viscito, L. Soft faults evaluation for electric heat pumps: Mechanistic models versus machine learning tools. In Proceedings of the 26th IIR International Congress of Refrigeration, Paris, France, 21–25 August 2023.
20. Pelella, F.; Viscito, L.; Mauro, A.W. Soft faults in residential heat pumps: Possibility of evaluation via on-field measurements and related degradation of performance. *Energy Convers. Manag.* **2022**, *260*, 115646. [CrossRef]
21. Ertesvåg, I.S. Uncertainties in heat-pump coefficient of performance (COP) and exergy efficiency based on standardized testing. *Energy Build.* **2011**, *43*, 1937–1946. [CrossRef]
22. Tran, C.T.; Rivière, P.; Marchio, D.; Arzano-Daurelle, C. Refrigerant-based measurement method of heat pump seasonal performances. *Int. J. Refrig.* **2012**, *35*, 1583–1594. [CrossRef]
23. Davis, J.M.; Martinkauppi, I.; Witte, H.; Berglöf, K.; Vallin, S. *IEA HPT Annex 52-Long-Term Performance Monitoring of GSHP Systems for Commercial, Institutional, and Multi-Family Buildings, Guidelines for Instrumentation and Data*; IEA: Paris, France, 2021.
24. Zhang, Y.; Akkurt, N.; Yuan, J.; Xiao, Z.; Wang, Q.; Gang, W. Study on model uncertainty of water source heat pump and impact on decision making. *Energy Build.* **2020**, *216*, 109950. [CrossRef]
25. Zhang, Y.; Cui, C.; Yuan, J.; Zhang, C.; Gang, W. Quantification of model uncertainty of water source heat pump and impacts on energy performance. *IOP Conf. Ser. Earth Environ. Sci.* **2019**, *238*, 012067. [CrossRef]
26. Kim, W.; Braun, J.E. Evaluation of the impacts of refrigerant charge on air conditioner and heat pump performance. *Int. J. Refrig.* **2012**, *35*, 1805–1814. [CrossRef]
27. Högberg, M.; Vamling, L. Impact of uncertainties on estimations of heat pump cycle performance. *Int.-Al J. Refrig.* **1996**, *19*, 34–42. [CrossRef]
28. *EN 14511-3:2022*; Air Conditioners, Liquid Chilling Packages and Heat Pumps for Space Heating and Cooling and Process Chillers, with Electrically Driven Compressors. Part 3: Test Methods. European Committee for Standardization: Brussels, Belgium, 2022.
29. Mauro, A.W.; Napoli, G.; Pelella, F.; Viscito, L. Flow pattern, condensation and boiling inside and outside smooth and enhanced surfaces of propane (R290). State of the art review. *Int. J. Heat Mass Transf.* **2021**, *174*, 121316. [CrossRef]
30. Luz, A.P.; Diniz, H.A.G.; Duarte, W.M.; Machado, L. Experimental study and semi-empirical model of a thermo-static expansion valve of a R290 direct-expansion solar heat pump. *Int. J. Refrig.* **2024**, *163*, 56–70. [CrossRef]
31. Mauro, A.W.; Passarelli, A.F.; Pelella, F.; Viscito, L. Sizing, safety, lifetime performance, environmental impact and costs of residential A-to-A heat pumps: Current and future scenarios according to new F-GAS regulation and EPBD. *Energy Build.* **2025**, *343*, 115896. [CrossRef]
32. *ASHRAE 41.2-2022*; Standard Methods for Air Velocity and Airflow Measurements. American Society of Heating, Refrigerating and Air-Conditioning Engineers: Peachtree Corners, GA, USA, 2022. Available online: https://www.equipmentnorm.com/ASHRAE/143379185/ASHRAE-41.2 (accessed on 6 February 2026).
33. Yu, F.W.; Chan, K.T.; Chu, H.Y. Constraints of using thermostatic expansion valves to operate air-cooled chillers at lower condensing temperatures. *Appl. Therm. Eng.* **2006**, *26*, 2470–2478. [CrossRef]
34. Shah, R.K.; Sekulic, D.P. *Fundamentals of Heat Exchanger Design*; John Wiley & Sons: London, UK, 2003.

35. Shah, M.M. An improved and extended general correlation for heat transfer during condensation in plain tubes. *HVAC&R Res.* **2009**, *15*, 889–913. [CrossRef]
36. Dittus, F.W.; Boelter, L.M.K. Heat transfer in automobile radiators of the tubular type. *Univ. Calif. Publ. Eng.* **1930**, *2*, 443–461. [CrossRef]
37. Wang, C.C.; Chi, Y.Y. Heat transfer and friction characteristics of plain fin-and-tube heat exchangers: Part II. Correlation. *Int. J. Heat Mass Transf.* **2000**, *43*, 2693–2700. [CrossRef]
38. Amalfi, R.L. Two-Phase Heat Transfer Mechanisms within Plate Heat Exchangers: Experiments, Modeling and Simulations 6856. Ph.D. Thesis, Ecole Polytechnique Federale de Lausanne (EPFL), Lausanne, Switzerland, 2016.
39. Martin, H. A theoretical approach to predict the performance of chevron-type plate heat exchangers. *Chem. Eng. Process. Process Intensif.* **1996**, *4*, 301–310. [CrossRef]
40. Sekulic, D.P.; Shah, R.K.; Pignotti, A. A review of solution methods for determining effectiveness-NTU relationships for heat exchangers with complex flow arrangements. *Appl. Mech. Rev.* **1999**, *52*, 97–117. [CrossRef]
41. Rouhani, S.Z.; Axelsson, E. Calculation of Void Volume Fraction in the Subcooled and Quality Boiling Regions. *Int. J. Heat Mass Transf.* **1970**, *13*, 383–393. [CrossRef]
42. *MATLAB R2024b*, The MathWorks, Inc.: Natick, MA, USA, 2024.
43. Lemmon, E.W.; Huber, M.L.; McLinden, M.O. *REFPROP, NIST Standard Reference Database 23*, version 9.0; National Institute of Standards and Technology: Gaithersburg, MD, USA, 2007.
44. D'Ignazi, C.; Molinaroli, L.; Bongiorno, C. Experimental study of the performance of a water-to-water heat pump equipped with a liquid receiver with different charge levels. *Int. J. Refrig.* **2024**, *168*, 688–695. [CrossRef]
45. Botticella, F.; De Rossi, F.; Mauro, A.W.; Vanoli, G.P.; Viscito, L. Multi-criteria (thermodynamic, economic and environmental) analysis of possible design options for residential heating split systems working with low GWP refrigerants. *Int. J. Refrig.* **2018**, *87*, 131–153. [CrossRef]
46. Navarro, E.; Granryd, E.; Urchueguía, J.F.; Corberán, J.M. A phenomenological model for analyzing reciprocating compressors. *Int. J. Refrig.* **2007**, *30*, 1254–1265. [CrossRef]
47. *JCGM 100:2008*; Evaluation of Measurement Data—Guide to the Expression of Uncertainty in Measurement. Joint Committee for Guides in Metrology: Sèvres, France, 2008.
48. McKay, M.D.; Beckman, R.J.; Conover, W.J. A comparison of three methods for selecting values of input variables in the analysis of output from a computer code. *Technometrics* **2000**, *42*, 55–61. [CrossRef]

Disclaimer/Publisher's Note: The statements, opinions and data contained in all publications are solely those of the individual author(s) and contributor(s) and not of MDPI and/or the editor(s). MDPI and/or the editor(s) disclaim responsibility for any injury to people or property resulting from any ideas, methods, instructions or products referred to in the content.